

## Solid-state dimer method for calculating solid-solid phase transitions

Penghao Xiao,<sup>1</sup> Daniel Sheppard,<sup>2</sup> Jutta Rogal,<sup>3</sup> and Graeme Henkelman<sup>1,a)</sup>

<sup>1</sup>Department of Chemistry and the Institute for Computational and Engineering Sciences, University of Texas at Austin, Austin, Texas 78712, USA

<sup>2</sup>Theoretical Division, Los Alamos National Laboratory, Los Alamos, New Mexico 87545, USA

<sup>3</sup>Interdisciplinary Centre for Advanced Materials Simulation, Ruhr-Universität Bochum, 44780 Bochum, Germany

(Received 13 March 2014; accepted 15 April 2014; published online 2 May 2014)

The dimer method is a minimum mode following algorithm for finding saddle points on a potential energy surface of atomic systems. Here, the dimer method is extended to include the cell degrees of freedom for periodic solid-state systems. Using this method, reaction pathways of solid-solid phase transitions can be determined without having to specify the final state structure or reaction mechanism. Example calculations include concerted phase transitions between CdSe polymorphs and a nucleation and growth mechanism for the A15 to BCC transition in Mo. © 2014 AIP Publishing LLC. [<http://dx.doi.org/10.1063/1.4873437>]

### I. INTRODUCTION

The harmonic approximation to transition state theory<sup>1,2</sup> is widely used to calculate reaction rates because it depends simply upon the energy difference between a local minimum and a saddle point connected to it by a steepest descent path. The dimer method is an efficient way to locate these first order saddle points on a given potential energy surface.<sup>3,4</sup> Different from the nudged elastic band method (NEB),<sup>5,6</sup> where both the reactant and product configurations are needed to find a connecting saddle point, the dimer method requires only initial configurations in the reactant state and can (in principle) find all connected saddles defining the possible escape pathways from the state. The corresponding product states are identified by minimizing configurations displaced along the negative mode of each saddle point found. Using dimer searches in each new state visited, the adaptive kinetic Monte Carlo (AKMC) algorithm has been developed to model kinetics and explore the connectivity of the thermally accessible region of the potential energy surface.<sup>7</sup> Possible reaction processes and rates are calculated on the fly based on the saddles found by the dimer method and the system is advanced from state-to-state by the kinetic Monte Carlo (KMC) algorithm.<sup>8,9</sup>

Within the dimer method the *dimer* consists of two configurations of the system separated by a small distance. The vector between the two images,  $\tau$ , is an estimate of the lowest curvature mode, which is used to bring the center of the dimer to a saddle point. There are two parts to the dimer method. First, the dimer is rotated about its center to minimize the total dimer energy and with this to find the lowest curvature mode. The rotation direction,  $\Theta$ , is along the force difference between the two images, with the component parallel to  $\tau$  projected out. The dimer energy is a sinusoidal function of the rotation angle on the plane spanned by  $\Theta$  and  $\tau$ , so the rotation angle which minimizes the dimer energy in this plane can be determined with a single additional force call.<sup>10,11</sup> Second,

the center of the dimer is translated by climbing up the potential energy surface along the lowest curvature mode direction and relaxing in all perpendicular directions. The dimer converges towards first order saddle points and is oriented along the negative curvature mode defining the reaction coordinate.

For solid-state systems, periodic boundary conditions are adopted to model infinite systems. Many solid-state reactions, and especially phase transitions, involve changes of both atomic positions and cell vectors. To correctly locate saddle point configurations in these systems, it is essential to treat all degrees of freedom on the same footing. Dragging along a chosen direction in a solid-state system, such as moving the cell first and then relaxing the atoms in a fixed cell, or vice versa, is not a reliable way to find saddle points.<sup>12,13</sup> Here, we show how the dimer algorithm can be extended to include the cell variables. In this solid-state dimer (SSD), both the cell and atomic degrees of freedom evolve in concert. The key to the method is the definition of an appropriate metric to define the distance between two structures so that the geometry of the configuration space is independent of the supercell used.

Our approach follows that of the solid-state nudged elastic band (SSNEB), which was developed using the same expanded degrees of freedom to locate saddle points of solid-solid phase transitions.<sup>12</sup> The limitation of any band type method is that both the initial and final configurations must be known to initiate the calculation, as well as a suitable initial interpolation between the two states. This is not a problem when studying simple diffusion mechanisms but the complexity of phase transitions makes this constraint a major limitation. In the NEB, the identity of each atom in the initial state must correspond uniquely to a specific atom in the final state. This atomic mapping creates a combinatorial explosion of possible final states with system size, differing only by atom identity. Moreover, the choice of unit cell for each state is not unique, which further increases the complexity of the mapping. The SSD method circumvents the atom permutation and cell variation issues by automatically following the atoms along the path they naturally take to saddle points and

<sup>a)</sup>henkelman@cm.utexas.edu

adjacent minima. Then, combined with the AKMC method, the SSD is able to automatically discover new crystal structures and new phase transformation mechanisms.

## II. METHODOLOGY

### A. Generalized cell and atom configuration space

The energy of a solid-state system represented with periodic boundary conditions is defined by the atomic positions  $\mathbf{r}$  and the cell matrix  $\mathbf{h}$  (with the cell vectors as rows). In the SSD, we aim to treat both types of variables in a single generalized space of atomic and cell coordinates. Changes in the cell vectors are naturally described in terms of strains which have different units from the atomic positions. A Jacobian, or metric, is required to combine them into a generalized displacement vector,

$$\Delta \mathbf{R} = \{J\boldsymbol{\epsilon}, \Delta \mathbf{r}\}. \quad (1)$$

Here,  $J$  is the Jacobian,  $\boldsymbol{\epsilon} = \mathbf{h}^{-1} \Delta \mathbf{h}$  is the strain, and  $\Delta \mathbf{r}$  is the change in the atomic positions in Cartesian coordinates. The strain is calculated with respect to the undeformed cell geometry. It could also be calculated with respect to the deformed cell,  $\boldsymbol{\epsilon} = (\mathbf{h} + \Delta \mathbf{h})^{-1} \Delta \mathbf{h}$ , but this distinction is not important for the metric because the two expressions for  $\boldsymbol{\epsilon}$  converge in the limit of  $\Delta \mathbf{h} \rightarrow 0$ , where the differential properties of the space are defined.

Note that the cell vectors  $\mathbf{h}$  and strain  $\boldsymbol{\epsilon}$  are both  $3 \times 3$  matrices, and the atomic displacements  $\Delta \mathbf{r}$  are  $N \times 3$  matrices, where  $N$  is the number of atoms in the supercell. Vectors in the generalized space,  $\Delta \mathbf{R}$  are therefore  $(N + 3) \times 3$  matrices. These dimensions are not, however, important for the SSD; dot products and norms are all calculated with flattened vectors.<sup>12</sup>

To separate atomic and cell changes, it is important to define the atomic motion in relative coordinates with respect to the cell vectors. In this way, a pure strain  $\boldsymbol{\epsilon}$  in the generalized space does not contribute to a change in the atomic coordinates  $\Delta \mathbf{r}$ . The separation of cell and atomic variables is accomplished by calculating  $\Delta \mathbf{r}$  as fractional changes along the cell coordinates, converted into Cartesian displacements. As with the calculation of  $\boldsymbol{\epsilon}$ ,  $\mathbf{h}$  is chosen as the reference cell for this transformation.

The most important issue for defining the space of cell vectors and atomic positions is the choice of Jacobian. The Jacobian provides the appropriate metric to combine strain and atom motion into a single vector. Our principle for choosing  $J$  is that the overall size and shape of the supercell should not affect the calculation of distances in our generalized space. Our choice of  $J$  is

$$J = \sqrt{N}L, \quad (2)$$

$$L = \left(\frac{\Omega}{N}\right)^{1/3}, \quad (3)$$

where  $N$  is the number of atoms in the supercell,  $L$  is the average distance between atoms calculated from the average volume, and  $\Omega$  is the volume of the supercell.  $J$  has units of length, which compensates for the fact that  $\boldsymbol{\epsilon}$  is unitless.  $J$  is

only calculated once in the initialization of the calculation and kept constant thereafter. A constant  $J$  is sufficient because the precise value is not as important as how  $J$  scales with system size. Furthermore, the saddle points are stationary and invariant to the choice of Jacobian.

A distance in the generalized configuration space is

$$\|\Delta \mathbf{R}\| = \sqrt{NL^2\|\boldsymbol{\epsilon}\|^2 + \|\Delta \mathbf{r}\|^2}. \quad (4)$$

One can see from this expression how  $J$  balances the relative weight between strain  $\boldsymbol{\epsilon}$  and atomic displacements  $\Delta \mathbf{r}$ . Consider, for example, a cell that is expanded into a supercell while maintaining the same atomic motion within each cell. The first term under the square root, corresponding to strain, increases linearly with the number of atoms in the cell, due to the  $\sqrt{N}$  term in  $J$  (Eq. (2)). The second term, corresponding to the atomic motion, also increases linearly with the number of atoms in the supercell. The Jacobian ensures that the ratio of the two terms remains the same, independent of the choice of supercell, resulting in a proportional change of the atomic and cell axes in the generalized space. It is trivial to prove that the dot product and angle between any two vectors also remain unchanged under different supercell representations, which confirms that the configuration space is undistorted.

Taking the first derivative of the energy with respect to  $\mathbf{R}$  gives the generalized force

$$\mathbf{F} = \left\{ \frac{\Omega}{J} \boldsymbol{\sigma}^{\text{cauchy}}, \mathbf{f} \right\}, \quad (5)$$

where  $\mathbf{f}$  are the atomic forces and  $\boldsymbol{\sigma}^{\text{cauchy}}$  is the Cauchy stress. One can verify that  $\mathbf{F} \cdot \Delta \mathbf{R}$  is the energy difference due to the displacement  $\Delta \mathbf{R}$ . The SSD can be extended to include external stress in an enthalpy landscape by modifying Eq. (5) to

$$\mathbf{F} = \left\{ \frac{\Omega}{J} (\boldsymbol{\sigma}^{\text{cauchy}} + \boldsymbol{\sigma}^{\text{external}}), \mathbf{f} \right\}. \quad (6)$$

### B. Solid-state dimer method

The dimer is defined by a point  $\mathbf{R}$  and a direction  $\boldsymbol{\tau}$ . In the generalized space of cell and atomic degrees of freedom  $\mathbf{R}$  has two components,  $\mathbf{h}$  and  $\mathbf{r}$ . As in Eq. (1), the direction is defined as  $\boldsymbol{\tau} = \{\boldsymbol{\tau}_\epsilon, \boldsymbol{\tau}_r\}$ , where  $\boldsymbol{\tau}_\epsilon$  and  $\boldsymbol{\tau}_r$  are the components from strain and atomic motions, respectively. The dimer can also be defined by its two end points, i.e., the two images of the system at  $\mathbf{R}_1$  and  $\mathbf{R}_2$ , which are centered about  $\mathbf{R}$  and separated along  $\boldsymbol{\tau}$  by a small distance  $\|\Delta \mathbf{R}\|$ .  $\mathbf{R}_1$  is calculated from  $\mathbf{R}$  and  $\boldsymbol{\tau}$  in the following way. First, the cell at the end-point,  $\mathbf{h}_1$ , is calculated as

$$\boldsymbol{\epsilon} = \frac{\|\Delta \mathbf{R}\|}{J} \boldsymbol{\tau}_\epsilon, \quad (7)$$

$$\mathbf{h}_1 = \mathbf{h}\boldsymbol{\epsilon} + \mathbf{h}. \quad (8)$$

Under the strain  $\boldsymbol{\epsilon}$ , the Cartesian atomic positions are scaled from  $\mathbf{r}$  to a new position vector that we will call  $\mathbf{r}'$ . Note that the relative atomic coordinates in these cells are constant,

when expressed as fractions of the cell vectors. After transforming to the new cell, the atomic positions are updated according to  $\tau_r$ ,

$$\mathbf{r}_1 = \mathbf{r}' + \|\Delta\mathbf{R}\|\tau_r. \quad (9)$$

With these definitions of generalized vectors, forces, and displacements, the rest of the SSD method is the same as the regular dimer method.<sup>3,10,11</sup> The dimer direction  $\tau$  is rotated according to the force differences between the two images; at the new orientation the end point is updated and the new forces are calculated; after  $\tau$  converges to the lowest curvature mode direction, the center of dimer is translated up the potential along  $\tau$  and down the potential in all other directions, using any force-based optimizer, until a saddle point is found. We note that the dimer rotation is equivalent to the Raleigh-Ritz optimization<sup>14</sup> that is used in the hybrid eigenvector following method,<sup>15</sup> and the more recent and closely related gentlest ascent dynamics method.<sup>16</sup>

### III. RESULTS

The SSD method is implemented as an extension of the atomic simulation environment (ASE) in the companion transition state (TSASE) code.<sup>17,18</sup> Exploration of the potential energy surface is done using the AKMC method<sup>7,19</sup> as implemented in the EON simulation package.<sup>20</sup> We use high temperature state-to-state AKMC dynamics to facilitate crossing of high barriers and sampling of both low and high energy crystal structures.

Two examples are used to demonstrate the capabilities of the SSD method. In the first example, we revisit the CdSe system previously explored with the SSNEB.<sup>12</sup> In addition to the transition pathways found with the SSNEB, the SSD finds many new structures which are illustrated in a disconnectivity graph.<sup>21</sup> In the second example, we calculate a phase transition between the A15 and BCC structures in Mo. With the SSD, two concerted mechanisms of the phase transition are found, without an assumed path or input from molecular dynamics. Finally, we combine the SSD and the SSNEB methods into an efficient strategy for discovering and refining reaction mechanisms. A small supercell representation serves as a coarse-grained model of the system which can be quickly explored by the SSD; the finer details along the pathway of interest, for example, at the interfaces between phases, are then refined with the SSNEB.

#### A. CdSe energy landscape

Our first example is the CdSe system with eight atoms in the supercell, which we have studied using the SSNEB method in a previous paper.<sup>12</sup> The same empirical potential, consisting of long range Coulomb and short range Lennard-Jones terms, describes the atomic interactions.<sup>22</sup> The initial structures for SSD searches are generated by the EON server with random displacements in the generalized space around the wurtzite (WZ) minimum. After the saddles around the minimum are found, the EON server builds a table of reaction rates based upon harmonic transition state theory, and advances the system to a new state with the KMC algorithm.

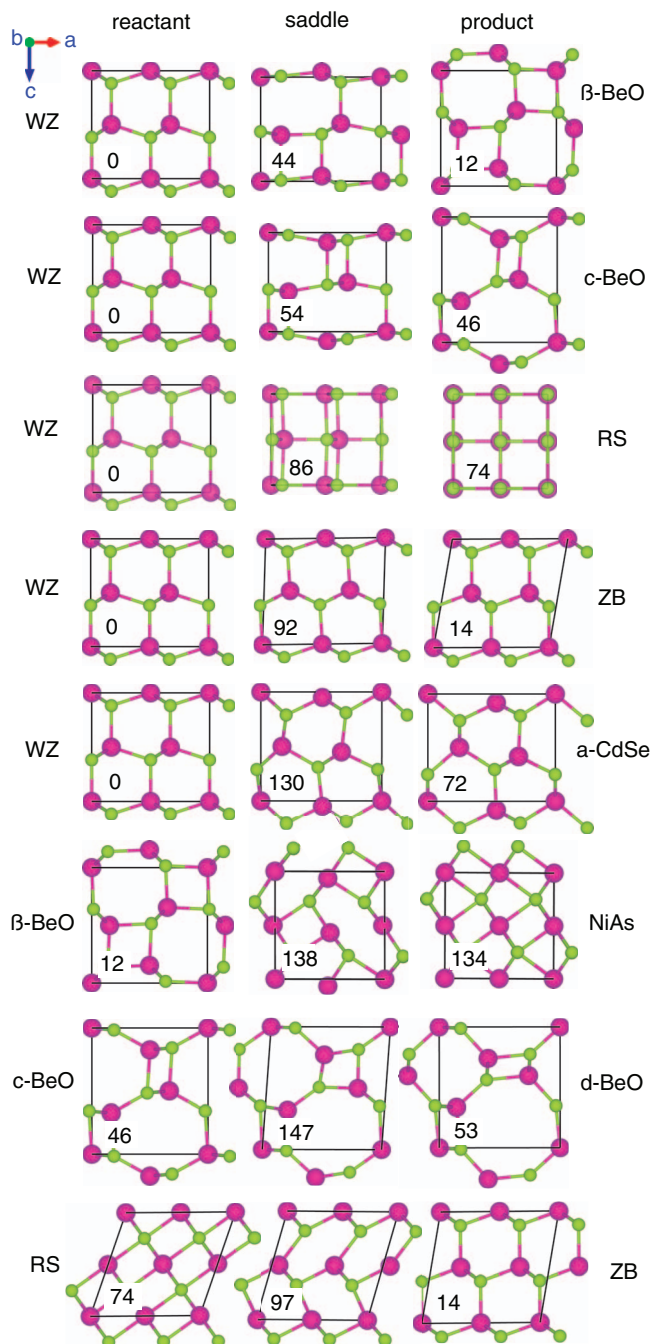


FIG. 1. Several phase transition mechanisms found by the SSD. Energy values are in meV/atom with respect to the lowest-energy WZ structure. Abbreviations of the structures are defined in the main text. The purple circles are Cd and the green are Se.

A high temperature of 5000 K is used to explore the network of stable crystal structures.

A selected set of saddle points and final state crystal phases found by the SSD are shown in Fig. 1. Interestingly, two concerted mechanisms were found for the WZ to rock salt (RS) transition. Fig. 2 illustrates both the lower energy path (I), shown in Fig. 1, and a slightly higher energy path (II). In path I, the cell contracts first along the  $c$ -axis and then along the  $a$ -axis; in path II, the cell has contracted both along the  $a$ - and  $c$ -axes at the saddle point. This example illustrates a strength of single-ended saddle search methods which are

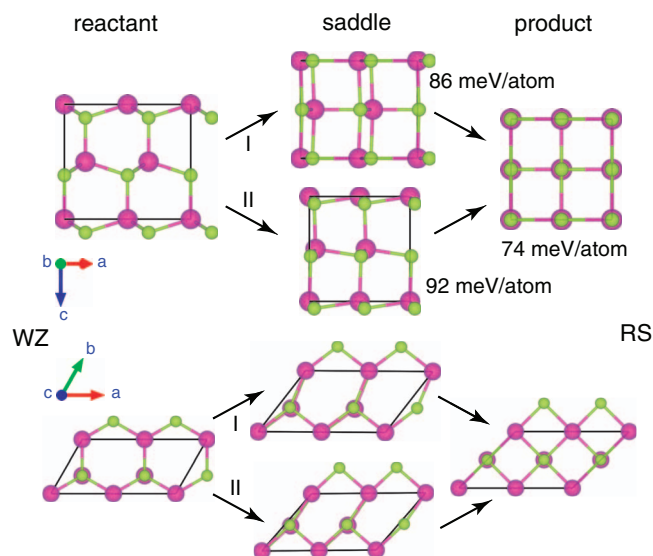


FIG. 2. Top and side views of two pathways from the wurtzite (WZ) to rock salt (RS) structure. Remarkably, there is the same atomic mapping between the reactant and product states in both mechanisms.

not biased to a particular path between an initial and final state. By contrast, the SSNEB, using an initial linear interpolation between the two states, would find only one of these pathways.

The resulting energy landscape is shown in the disconnectivity graph in Fig. 3(a). The most interesting high symmetry and low energy structures were relaxed with density functional theory (DFT) calculations,<sup>23</sup> yielding the energy landscape shown in Fig. 3(b). The DFT calculations were performed with the Vienna *ab initio* simulation package (VASP) using the PW91 exchange-correlation functional and a basis set of plane waves with an energy cutoff of 350 eV.<sup>24–26</sup> The projector augmented wave method modeled the core electrons.<sup>27,28</sup> All of the stable structures found with the empirical potential were also found to be distinct minima when fully relaxed in DFT. Transition states between the minima were calculated using the SSNEB within the VASP code, using the minimum energy paths (MEPs) from the empirical potential to initialize the DFT calculations.

The palm-tree shape of the energy landscape calculated with the empirical potential remains intact with DFT, but the lowest barrier to escape the WZ phase increases significantly and the RS and NiAs branches become less stable within the tree. Overall, the empirical potential gives reliable structures over the range of local minima as well as reasonable relative energy differences between them. The phase transition barriers, however, deviate significantly from the DFT results. A good compromise can be made by finding structures and pathways with the empirical potential and then refining the energetics with DFT.

Finding new crystal structures in this way can be useful for screening of materials with interesting properties. The energy landscape also provides information about which materials can be synthesized.<sup>29</sup> The WZ and zinc blende (ZB) are the two structures that are observed in experiments at low temperature and pressure. The funneled “palm-tree” energy landscape explains why the two lowest energy states, WZ and ZB, are relatively easy to synthesize by annealing. The NiAs structure has also been observed in a constant pressure molecular dynamics simulation, but it may be difficult to stabilize under experimental conditions due to the shallowness of its basin of attraction.<sup>30</sup> The d-BeO and a-CdSe structures have not been reported before. Their basins of attraction are deep, but the entrances are relatively high in the energy funnel. If these entrances are bypassed at high temperature, the chances to visit the d-BeO and a-CdSe structures by annealing will be low.

## B. A combined dimer and NEB approach to find complex pathways

Typically, we are interested in phase transitions between stable crystal structures in which the end points can be fully represented by a small supercell. The SSD efficiently finds concerted mechanisms of phase transitions in small cells, but these may not be sufficient to describe the details of a real transition process, such as one involving nucleation and growth.<sup>31</sup> As the cell size is increased, complex and local mechanisms can be resolved, but it becomes increasingly difficult for the SSD to find complete phase transition pathways in the high dimensional configuration space.

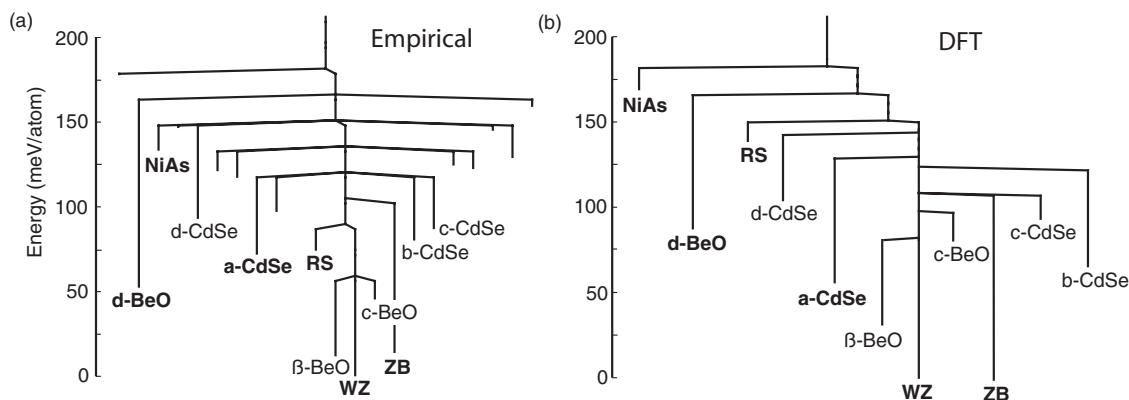


FIG. 3. A disconnectivity graph of the eight atom CdSe system calculated with (a) an empirical potential and (b) density functional theory. Several of the ordered low energy structures are labelled.

A natural compromise between the mechanistic limitations of a small cell and the computational cost of a large cell can be achieved by combining the SSD and SSNEB methods. We start with a small cell and use the SSD to find interesting concerted transitions. Then the SSNEB is used with a larger supercell to allow for local relaxation along the path found by the SSD. Small random displacements are made to the atoms in the SSNEB calculations in order to break the symmetry of the concerted processes found by the SSD. In this way, the coarse grained mechanisms are found by the SSD and the fine grained mechanistic details, including local nucleation and growth, are resolved by the SSNEB.

### C. A15 to BCC solid-solid transformation in Mo

In our second example we show how the SSD can be combined with the SSNEB to efficiently discover and refine details of a complex transformation process in bulk Mo. Complex crystal structures, such as the A15 phase, can form in metal alloys with high concentrations of refractory elements (e.g., Mo) and significantly influence their mechanical properties.<sup>32</sup> There is, however, little understanding of the atomistic mechanisms underlying the formation of these phases. The A15 phase is usually only observed in binary or multicomponent alloys, but elemental Mo is a good model system for this work since theoretical studies showed that in Mo the A15 phase is only slightly less stable than and thus competing with the BCC ground state.<sup>33,34</sup> Furthermore there is an embedded atom method potential for Mo<sup>35</sup> that gives reasonable bulk properties for BCC and A15 as well as an appropriate value for the energy difference between the two phases. To investigate the possible transition paths, we ran several hundreds of SSD searches initiated by making random displacements to all degrees of freedom in the A15 structure. Two concerted mechanisms were found as shown in Fig. 4. In both cases, atomic and cell motions are significant.

Based on the first concerted path in Fig. 4, we expand the supercell of the initial and final structures and use the SSNEB to refine the MEP. This cell is expanded into a  $5 \times 5 \times 1$  supercell within the plane shown in Fig. 4. In this way, we are looking at a quasi-2D system with a periodic unit cell in the perpendicular direction. The converged MEP is shown in

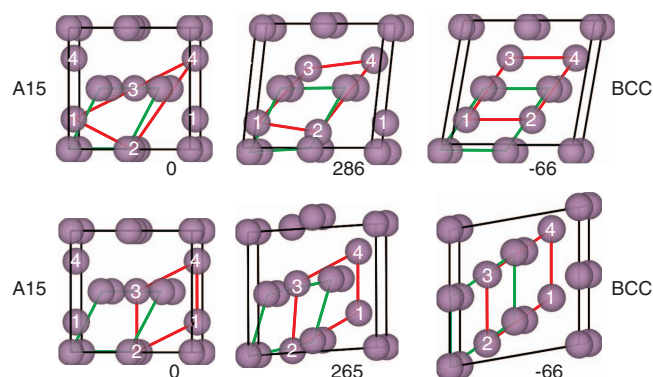


FIG. 4. Two concerted mechanisms of the A15 to BCC phase transition in Mo. The moving atoms are labeled, and the two sub-lattices outlined for visualization purposes. Energies, listed below each structure, are in meV/atom.

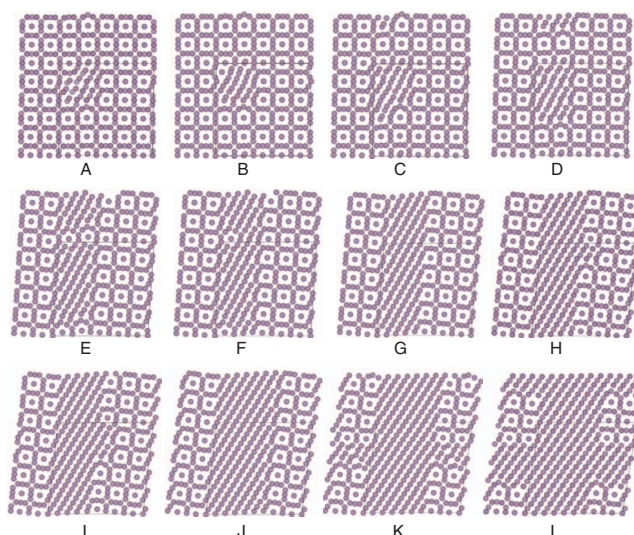
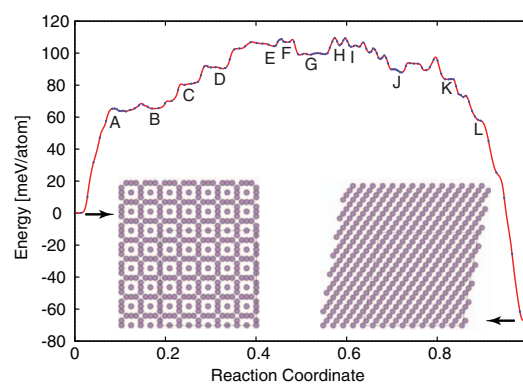


FIG. 5. A localized nucleation and growth mechanism for the A15 to BCC phase transition in Mo as calculated in a  $5 \times 5 \times 1$  supercell by the SSNEB method. Several metastable structures along the MEP are shown.

Fig. 5. In the larger supercell, the initial path, taken to be the concerted mechanism found by the SSD, relaxes to a lower energy local transition in which the BCC phase nucleates locally and propagates throughout the cell. The overall barrier along the path is reduced from 286 meV/atom in the concerted mechanism to 109 meV/atom in the local mechanism. We note, however, that the barriers for the concerted and local mechanisms cannot be compared directly, since they scale differently with system size; the former with the volume of the system and the latter with the area of the A15-BCC interface. By choosing a large enough supercell, the concerted mechanism can be relaxed with the SSNEB to a lower energy nucleation and growth mechanism.<sup>12</sup>

The nucleus of the new phase forms in the middle of configuration (A) with a sharp increase in energy. In (B) the nucleus takes a clear BCC structure. The BCC phase then grows along the vertical direction unit cell by unit cell following atomic motion similar to that shown in Fig. 4. The energy increases as the nucleus grows. In principle, the state with the highest energy corresponds to the critical nucleus, but in this simulation the critical size is not reached before the nucleus spans the periodic boundary, in (F). From (G), the BCC phase grows along the two phase boundary and the energy drops due to the relative stability of BCC over A15 and the fact that the overall length of the boundary barely increases. From (G) to

(J) a complete layer of A15 is converted into BCC, one unit cell at a time. After (J), the BCC growth mechanism is again affected by the periodic boundary conditions. Configuration (L) can be viewed as an A15 nucleus, which is relatively unstable with respect to the final pure BCC phase.

#### IV. CONCLUSION

The SSD method is designed to find saddle points in the generalized configuration space of both atomic and cell degrees of freedom. The method is demonstrated to find phase transitions between different crystal structures represented under periodic boundary conditions. Combined with the AKMC server in EON, the energy landscape of CdSe is calculated in the form of a disconnectivity graph. In this way, the discovery of new phases, as well as a determination of their stability is possible, which is a helpful guide for synthesis. More complex mechanisms involving both local atomic motion and collective shifts in the cell can be found with a combination of the SSD and SSNEB methods. The SSD efficiently finds collective transformation mechanisms in a small supercell and the SSNEB is able to refine the path in terms of local atomic motion along the path. This hybrid approach is used to determine a quasi-2D nucleation and growth pathway for the Mo A15-BCC phase transition.

#### ACKNOWLEDGMENTS

The method development work was supported by the National Science Foundation under Grant No. CHE-1152342, and the calculations were supported as part of the program “Understanding Charge Separation and Transfer at Interfaces in Energy Materials (EFRC:CST)” an Energy Frontier Research Center funded by the U.S. Department of Energy, Office of Science, Office of Basic Energy Sciences under Award No. DE-SC0001091, and the Welch Foundation under Grant No. F-1841. Calculations were done with resources from the National Energy Research Scientific Computing Center and the Texas Advanced Computing Center. We would like to thank Rye Terrell, Ari Harjunmaa, and Ralf Drautz for helpful discussions and related research on the A15 to BCC phase transition.

- <sup>1</sup>C. Wert and C. Zener, *Phys. Rev.* **76**, 1169 (1949).
- <sup>2</sup>G. H. Vineyard, *J. Phys. Chem. Solids* **3**, 121 (1957).
- <sup>3</sup>G. Henkelman and H. Jónsson, *J. Chem. Phys.* **111**, 7010 (1999).
- <sup>4</sup>R. A. Olsen, G. J. Kroes, G. Henkelman, A. Arnaldsson, and H. Jónsson, *J. Chem. Phys.* **121**, 9776 (2004).
- <sup>5</sup>G. Henkelman, B. P. Uberuaga, and H. Jónsson, *J. Chem. Phys.* **113**, 9901 (2000).
- <sup>6</sup>G. Henkelman and H. Jónsson, *J. Chem. Phys.* **113**, 9978 (2000).
- <sup>7</sup>L. Xu and G. Henkelman, *J. Chem. Phys.* **129**, 114104 (2008).
- <sup>8</sup>A. B. Bortz, M. H. Kalos, and J. L. Lebowitz, *J. Comput. Phys.* **17**, 10 (1975).
- <sup>9</sup>D. T. Gillespie, *J. Comput. Phys.* **22**, 403 (1976).
- <sup>10</sup>A. Heyden, A. T. Bell, and F. J. Keil, *J. Chem. Phys.* **123**, 224101 (2005).
- <sup>11</sup>J. Kästner and P. Sherwood, *J. Chem. Phys.* **128**, 014106 (2008).
- <sup>12</sup>D. Sheppard, P. Xiao, W. Chemelewski, D. D. Johnson, and G. Henkelman, *J. Chem. Phys.* **136**, 074103 (2012).
- <sup>13</sup>K. J. Caspersen and E. A. Carter, *Proc. Natl. Acad. Sci. U.S.A.* **102**, 6738 (2005).
- <sup>14</sup>R. A. Horn and C. R. Johnson, *Matrix Analysis* (Cambridge University Press, Cambridge, 1985).
- <sup>15</sup>L. J. Munro and D. J. Wales, *Phys. Rev. B* **59**, 3969 (1999).
- <sup>16</sup>W. E and X. Zhou, *Nonlinearity* **24**, 1831 (2011).
- <sup>17</sup>See <https://wiki.fysik.dtu.dk/ase/> for information about the ASE project.
- <sup>18</sup>See <http://theory.cm.utexas.edu/henkelman/code/> to obtain the TSASE code.
- <sup>19</sup>G. Henkelman and H. Jónsson, *J. Chem. Phys.* **115**, 9657 (2001).
- <sup>20</sup>S. T. Chill, M. Welborn, R. Terrell, L. Zhang, J.-C. Berthet, A. Pedersen, H. Jónsson, and G. Henkelman, “EON: Software for long time simulations of atomic scale systems,” *Model. Simul. Mater. Sci. Eng.* (in press).
- <sup>21</sup>O. M. Becker and M. Karplus, *J. Chem. Phys.* **106**, 1495 (1997).
- <sup>22</sup>E. Rabani, *J. Chem. Phys.* **116**, 258 (2002).
- <sup>23</sup>W. Kohn, A. D. Becke, and R. G. Parr, *J. Phys. Chem.* **100**, 12974 (1996).
- <sup>24</sup>G. Kresse and J. Furthmüller, *Comput. Mater. Sci.* **6**, 15 (1996).
- <sup>25</sup>G. Kresse and J. Furthmüller, *Phys. Rev. B* **54**, 11169 (1996).
- <sup>26</sup>J. P. Perdew, in *Electronic Structure of Solids*, edited by P. Ziesche and H. Eschrig (Akademie Verlag, Berlin, 1991), pp. 11–20.
- <sup>27</sup>P. E. Blöchl, *Phys. Rev. B* **50**, 17953 (1994).
- <sup>28</sup>G. Kresse and D. Joubert, *Phys. Rev. B* **59**, 1758 (1999).
- <sup>29</sup>M. Jansen, *Angew. Chem. Int. Ed.* **41**, 3746 (2002).
- <sup>30</sup>M. Grünwald, K. Lutker, A. P. Alivisatos, E. Rabani, and P. L. Geissler, *Nano Lett.* **13**, 1367 (2013).
- <sup>31</sup>P. Xiao and G. Henkelman, *J. Chem. Phys.* **137**, 101101 (2012).
- <sup>32</sup>C. M. F. Rae and R. C. Reed, *Acta Mater.* **49**, 4113 (2001).
- <sup>33</sup>C. Berne, A. Pasturel, M. Sluiter, and B. Vinet, *Phys. Rev. Lett.* **83**, 1621 (1999).
- <sup>34</sup>B. Seiser, T. Hammerschmidt, A. N. Kolmogorov, R. Drautz, and D. G. Pettifor, *Phys. Rev. B* **83**, 224116 (2011).
- <sup>35</sup>X. W. Zhou, H. N. G. Wadley, R. A. Johnson, D. J. Larson, N. Tabat, A. Cerezo, A. K. Petford-Long, G. D. W. Smith, P. H. Clifton, R. L. Martens *et al.*, *Acta. Mater.* **49**, 4005 (2001).